Atmos. Chem. Phys. Discuss., 15, 31665–31703, 2015
www.atmos-chem-phys-discuss.net/15/31665/2015/
doi:10.5194/acpd-15-31665-2015

Atmospheric Chemistry and Physics Discussions

Investigation of ice particle habits to be used for ice cloud remote sensing for the GCOM-C satellite mission

H. Letu[1], H. Ishimoto[2], J. Riedi[3], T. Y. Nakajima[1], L. C.-Labonnote[3], A. J. Baran[4], T. M. Nagao[5], and M. Skiguchi[6]

[1]Research and Information Center (TRIC), Tokai University, 4-1-1 Kitakaname Hiratsuka, Kanagawa 259-1292, Japan
[2]Meteorological Research Institute, Nagamine 1-1, Tsukuba 305-0052, Japan
[3]Laboratoire d'Optique Atmosphérique, UMR CNRS 8518, Université de Lille 1-Sciences et Technologies, Villeneuve d'Ascq, France
[4]Met Office, Fitzroy Road, Exeter, EX1 3PB, UK
[5]Earth Observation Research Center (EORC), Japan Aerospace Exploration Agency (JAXA), 2-1-1 Sengen Tsukuba-shi, Ibaraki 305-8505, Japan
[6]Tokyo University of Marine Science and Technology, Tokyo 135-8533, Japan

Received: 29 September 2015 – Accepted: 23 October 2015 – Published: 11 November 2015

Correspondence to: T. Y. Nakajima (nkjm@yoyogi.ycc.u-tokai.ac.jp)

Published by Copernicus Publications on behalf of the European Geosciences Union.

Abstract

Various ice particle habits are investigated in conjunction with inferring the optical properties of ice cloud for the Global Change Observation Mission-Climate (GCOM-C) satellite program. A database of the single-scattering properties of five ice particle habits, namely, plates, columns, droxtals, bullet-rosettes, and Voronoi, is developed. The database is based on the specification of the Second Generation Global Imager (SGLI) sensor onboard the GCOM-C satellite, which is scheduled to be launched in 2017 by Japan Aerospace Exploration Agency (JAXA). A combination of the finite-difference time-domain (FDTD) method, Geometric Optics Integral Equation (GOIE) technique, and geometric optics method (GOM) are applied to compute the single-scattering properties of the selected ice particle habits at 36 wavelengths, from the visible-to-infrared spectral region, covering the SGLI channels for the size parameter, which is defined with respect to the equivalent-volume radius sphere, which ranges between 6 and 9000. The database includes the extinction efficiency, absorption efficiency, average geometrical cross-section, single-scattering albedo, asymmetry factor, size parameter of an equivalent volume sphere, maximum distance from the center of mass, particle volume, and six non-zero elements of the scattering phase matrix. The characteristics of the calculated extinction efficiency, single-scattering albedo, and asymmetry factor of the five ice particle habits are compared.

Furthermore, the optical thickness and spherical albedo of ice clouds using the five ice particle habit models are retrieved from the Polarization and Directionality of the Earth's Reflectances-3 (POLDER-3) measurements on board the Polarization and Anisotropy of Reflectances for Atmospheric Sciences coupled with Observations from a Lidar (PARASOL). The optimal ice particle habit for retrieving the SGLI ice cloud properties was investigated by adopting the spherical albedo difference (SAD) method. It is found that the SAD, for bullet-rosette particle, with radii of equivalent volume spheres ($\widetilde{r}$) ranging between 6 to 10 µm, and the Voronoi particle, with $\widetilde{r}$ ranging between 28 to 38 µm, and 70 to 100 µm, is distributed stably as the scattering angle increases. It is

ACPD
15, 31665–31703, 2015

confirmed that the SAD of small bullet rosette and all sizes of voronoi particles has a low angular dependence, indicating that the combination of the bullet-rosette and Voronoi models are sufficient for retrieval of the ice cloud spherical albedo and optical thickness as an effective habit models of the SGLI sensor. Finally, SAD analysis based on the Voronoi habit model with moderate particles ($\widetilde{r} = 30\,\mu m$) is compared to the conventional General Habit Mixture (GHM), Inhomogeneous Hexagonal Monocrystal (IHM), 5-plate aggregate and ensemble ice particle model. It is confirmed that the Voronoi habit model has an effect similar to the counterparts of some conventional models on the retrieval of ice cloud properties from space-borne radiometric observations.

1 Introduction

Ice clouds play an important role in the radiation balance of the Earth's atmospheric system through interaction with solar radiation and infrared emission (Liou, 1986; Baran, 2012). However, there are still large uncertainties in characterizing their microphysical and optical properties. This is because they consist of ice particles with a wide range of habits and sizes (C.-Labonnote et al., 2000; Forster et al., 2007; Baran et al., 2009; Cole et al., 2014; Yang et al., 2015). Different ice particle habits have varying single-scattering characteristics, resulting in different radiative properties. The only feasible way of inferring ice cloud properties on a global scale is to use satellite observations. In practice, an ice model is chosen, which may consist of a single habit or a mixture of habits, and look-up tables (LUTs) for ice cloud reflection and transmission characteristics are computed for a range of input optical properties, particularly, optical thickness, cloud temperature, and effective particle size. The LUTs and a fast radiative transfer model are used subsequently for global operational retrievals. Thus, the choice of an ice model for a given satellite mission deserves rigorous investigation. In this paper, the present study is to better understand the performance of several ice cloud habit models, in conjunction with applications to the Global Change Observation Mission-Climate (GCOM-C) satellite mission.

ACPD
15, 31665–31703, 2015

In the past two decades, aircraft and balloon in-situ observations and space-borne and ground-based remote sensing techniques have contributed greatly to understanding ice cloud microphysical and radiative properties (Baran et al., 1998, 1999, 2003; Heymsfield et al., 2002; Heymsfield, 2003; Zhang et al., 2009). A variety of ice particle models have been developed based on in-situ observations and the single-scattering properties continuously draw a great deal of interest, particularly, from the perspective of numerical computation (e.g., Macke et al., 1996a, b; McFarquhar and Heymsfield, 1996; Yang et al., 2000, 2005, 2013; Um and McFarquhar, 2007, 2009, 2011; Nousiainen et al., 2011; Baum et al., 2005, 2011; Baran and C.-Labonnote, 2007; Ishimoto et al., 2012b; Liu et al., 2014). Light scattering computation methods include the finite-difference time-domain (FDTD) method (Yee, 1966; Yang and Liou, 1998a; Sun et al., 1999; Ishimoto et al., 2012a), **T**-matrix (Havemann and Baran, 2001; Bi and Yang, 2014), the discrete dipole approximation (DDA) method (Purcell and Pennypacker, 1973; Draine and Flatau, 1994; Yurkin et al., 2007), the pseudo-spectral time-domain (PSTD) method (Liu et al., 1997, 1998, 2012; Chen et al., 2008), the surface-integral equation method (SIEM; Nakajima et al., 2009), the improved geometric optics method (IGOM) (Yang and Liou, 1996), and the ray-tracing geometric optics method (GOM) (Takano, 1989, 1993; Macke, 1993; Macke et al., 1996a; Yang and Liou, 1998b; Masuda et al., 2012).

Based on one or more of these scattering models, single-scattering property libraries have been developed for certain habits. Hess et al. (1994) developed the single-scattering properties database for hexagonal plates and columns with a random orientation at wavelengths between 0.35 and 3.7 µm. Yang et al. (2000) developed a scattering and absorption property database for various ice particle habits with random orientation using the FDTD and IGOM methods, at wavelengths between 0.2 and 5 µm. Six different ice particle habits were selected in the calculations: plates, solid and hollow columns, planar bullet-rosettes, spatial bullet-rosettes, and aggregates. Yang et al. (2005) published the database for ice particles with eight different habits at 49 wavelengths between 3 and 100 µm, using a combination of several methods, includ-

ACPD
15, 31665–31703, 2015

ing the FDTD, **T**-matrix, IGOM, and Lorenz–Mie theory. Recently, Yang et al. (2013) released a full set of scattering, absorption, and polarization properties assuming random orientation for a set of 11 habits at a number of wavelengths, ranging between 0.2 and 100 µm. The habits include droxtals, prolate spheroids, oblate spheroids, solid and hollow columns, and compact ice aggregates which were composed of eight solid hexagonal ice columns (hereafter, "8-column aggregate", hexagonal plates, small spatial aggregates composed of 5 plates (hereafter, "5-plate aggregate"), large spatial aggregates, composed of 10 plates, and solid and hollow bullet-rosettes. This library is based on the Amsterdam discrete dipole approximation (ADDA), **T**-matrix, and IGOM methods. Based on this updated library, Baum et al. (2014) developed a new set of bulk scattering and absorption models with habit mixtures for use in ice cloud radiative transfer calculations and retrieval of the ice cloud properties from remote sensing measurements. The ice crystal single-scattering databases of Baran and Francis (2004) and Baran et al. (2014) have been constructed from numerical simulations of individual ice crystals by using a combination of methods described in those papers.

This study is aimed at identifying an optimal choice of ice habits for the Global Change Observation Mission (GCOM-C) satellite mission. It is useful to provide a brief summary of what other teams have chosen for their operational products. Numerous articles have investigated the use of effective ice particle habits derived from various ice habit models and remote sensing measurements from multi-angles for use in cloud parameter retrievals (Baran et al., 1998, 1999, 2003; Chepfer, 1998; C.-Labonnote et al., 2000; Chepfer et al., 2001; Masuda et al., 2002; Knap et al., 2005; Sun et al., 2006; Baran and Labonnote, 2006). Baran et al. (2007). C.-Labonnote et al. (2000, 2001) and Doutriaux et al. (2000) developed models of randomly oriented hexagonal ice particles containing spherical air bubbles (inhomogeneous hexagonal monocrystal (IHM) model) for use in the ice cloud retrievals of the POLDER (POLarization and Directionality of the Earth's Reflectances) measurements. The spherical albedo difference (SAD) analysis is employed to investigate the capability of the IHM model for retrieving the optical property of ice cloud. It is illustrated that the POLDER multi-angle measurements is

ACPD
15, 31665–31703, 2015

sensitive to the ice particle habit and roughness, at least for ice clouds having an optical thickness larger than 5. Chepfer et al. (2002) investigated the effective ice particle habits using multi-angle and multi-satellite methods from visible reflectance satellite measurements. There is increasing evidence that the ice particle model should contain some degree of surface roughness (Foot, 1998; Baran et al., 2001, 2003; Ottaviani et al., 2012a; van Diedenhoven et al., 2012; Cole et al., 2013, 2014). Yi et al. (2013) reported that the general habit mixture model (GHM, Baum et al., 2011, 2014) provided significant differences in the shortwave cloud radiative effect in the National Center for Atmosphere Research Community Atmosphere Model (NCAR CAM 5). Baran and Labonnote (2007) developed an ensemble ice particle model for cirrus using various habits including single hexagonal columns, a six-branched bullet-rosette, and more complex three-branched, five-branched, eight-branched, and ten-branched particles. Baran et al. (2014) demonstrated that it is possible to simulate measured cirrus radiances from the UV to microwave frequencies by using the same microphysically consistent habit mixture model throughout the spectrum. At solar wavelengths, both Baran and Labonnote (2007) and Baran et al. (2014) showed that featureless phase functions best fitted their multi-angle solar radiance measurements. Moreover, Baran et al. (2015) investigated the relationship between the habit model of the cirrus cloud particles and the atmospheric relative humidity. These studies suggest that whatever ice model is employed, it should have a featureless phase function at solar wavelengths. Ishimoto et al. (2012b) developed a new habit of complex and highly irregular shapes called Voronoi aggregate, which was based on the ice particle images of convective ice clouds from in-situ measurements. The phase function of the Voronoi habit varies smoothly with scattering angle, which is similar behavior found from assuming severe surface roughness or including bubbles within the particle or a combination of included bubbles and surface roughness. However, the use of the Voronoi habit model for retrieval of the ice cloud optical thickness has not been investigated yet.

In this study, the single-scattering properties of the various ice particle models were calculated for developing the ice cloud property products of the GCOM-C Second Gen-

ACPD
15, 31665–31703, 2015

eration Global Imager (SGLI) satellite sensor. FDTD (Ishimoto et al., 2012a), GOIE (Ishimoto et al., 2012a) and GOM (Masuda et al., 2012) methods are used to calculate the light scattering properties for five ice habits including columns, plates, droxtals, bullet-rosettes, and Voronoi, for a set of SGLI wavelengths. The SAD analysis is performed to investigate the optimal habit(s) using the POLDER-3 data. Furthermore, the results of the SAD analysis of the Voronoi habit model are compared with the conventional GHM, the IHM model and 5-plate aggregate model of Yang et al. (2013).

2 Single-scattering properties of the ice particle for the SGLI sensor

Single-scattering properties for the five ice particle habits are calculated for the SGLI observation channels. The single-scattering properties are used to determine the optimal ice particle habits using the SAD method. The SGLI is the successor sensor to the Global Imager (GLI) on board ADEOS-II, which takes measurements at wavelengths ranging from the near ultraviolet to the thermal infrared (IR). The first satellite GCOM-C1 is scheduled for launch in 2017 by the Japan Aerospace Exploration Agency (JAXA). The GCOM-C mission intends to establish a long-term satellite-observing system to measure essential geophysical parameters on the Earth's surface and in the atmosphere on the global scale, to facilitate the understanding of the global radiation budget, carbon cycle mechanism and climate change (Imaoka et al., 2010). As shown in Table 1, SGLI has 19 channels, including two polarization channels at visible/near-infrared wavelengths. A detailed description of the SGLI is reported by Imaoka et al. (2010), Nakajima et al. (2011), and Letu et al. (2012).

Four of the ice particle habits (hexagonal columns, plates, bullet-rosettes, and droxtals) employed in this study were chosen by referring to MODIS collections-5 ice particle model (Baum et al., 2005) and ice cloud in-situ measurement data. The habits shown in Fig. 1 are defined with the same parameters (semi-width, length, aspect ratio and maximum dimension) as employed in the scattering properties database by Yang et al. (2000, 2005). The Voronoi habit is determined numerically by extraction

ACPD
15, 31665–31703, 2015

of Wigner-Seitz cells from a 3-D mosaic image of the ice cloud microphysical data (Ishimoto et al., 2012b); this habit is different from the aggregate model used in the scattering database reported by Yang et al. (1998b, 2013). Spatial Poisson–Voronoi tessellations were used to determine the complex structure of the ice particles for the 3-D mosaic image. The geometry of each cell in the Voronoi tessellation is defined and is based on the method by Ohser et al. (2000).

A combination of the FDTD, GOIE, and GOM methods is employed to calculate the single-scattering properties of these five ice habits for a wide range of size parameters (SZP). The refractive index of ice published by Warren and Brandt (2008) is used in the computations. As shown in Table 2, the FDTD method is used to calculate the single-scattering properties of ice particles with small size parameters (SZP < 50). The GOIE and GOM methods are employed for calculating the scattering properties of the ice particle with medium and large size parameters, respectively. The wavelength selected for detailed calculations is determined by optimizing the results of the scattering database for the SGLI channels (Letu et al., 2010). Calculations are performed at 27 spectral wavelengths (λ) from the visible to the IR spectral region in the SGLI channels shown in Table 2. The effective particle radius ($\tilde{r}$) ranges from 0.7 to 533 µm and the SZP ranges from 0.35 to 6098. The $\tilde{r}$ is defined as a single particle radius of equivalent volume sphere. The SZP is given as,

$$\mathrm{SZP} = 2\pi \cdot \tilde{r}/\lambda \quad (1)$$

Consideration of the edge effect (Bi et al., 2010, Bi and Yang, 2014) is important for calculating the extinction efficiency (Q_{ext}) and absorption efficiency (Q_{abs}) by the GOIE method when the size parameter is less than 1000. The treatment of the edge effect is based on the method proposed by Ishimoto et al. (2012a). Correction coefficients are calculated in this study from comparison results of the FDTD and GOIE as shown in Eq. (2):

$$Q_{\mathrm{ext}} = Q_{\mathrm{ext/GOIE}} + K_1 \cdot \mathrm{SZP}^{-2/3}, Q_{\mathrm{abs}} = Q_{\mathrm{abs/GOIE}} + K_2 \cdot \mathrm{SZP}^{-2/3} \quad (2)$$

ACPD
15, 31665–31703, 2015

where $Q_{ext/GOIE}$ and $Q_{abs/GOIE}$ are the extinction efficiencies, respectively, calculated by the GOIE method. K_1 and K_2 are the coefficients of the edge-effect contribution. These coefficients are applied to correct the Q_{ext} and Q_{abs} of large particles calculated using GOIE, which is calculated by comparing Q_{ext} and Q_{abs} obtained from FDTD and GOIE for maximum extension from the center of mass ranging from 30 to 60 µm.

3 Data and methods

Since 1996, three POLDER instruments have been flown to study clouds and aerosols with multiple angles and polarization capabilities. The POLDER-1 and POLDER-2 onboard ADEOS satellite of JAXA were operated from November 1996 to June 1997 and December 2002 to October 2003, respectively. Both of the POLDER instruments observed the intensity from 14 viewing directions with scattering angles from 60 to 180° . The spatial resolution of the product derived from POLDER-2 observation data is approximately 20 km, which is composed of 3 × 3 single pixels. POLDER-2 can measure the upwelling total and polarized radiances from eight observing channels centered at wavelengths of 0.443, 0.490, 0.565, 0.670, 0.763, 0.765, 0.865, and 0.910 µm (Baran et al., 2006). POLDER-3 onboard the Polarization and Anisotropy of Reflectances for Atmospheric Sciences coupled with Observations from a Lidar (PARASOL) microsatellite was launched in 2004. The POLDER-3 has nine observing channels, three of which have polarization capabilities. PARASOL/POLDER-3 views a given scene at up to 16 different angles as the satellite passes overhead. However, the capabilities of the instrument, such as observing the radiances from multi-viewing angles in several visible channels, are important for investigating the representative ice particle models for retrieving ice cloud properties. In this study, 589 246 pixels of the POLDER-3 observation data with a global scale over ocean from days 20–22 March, June, September, and December 2008 are used to retrieve cloud optical thickness and spherical albedo for investigating the behavior of the five ice particle habits. Figure 2a shows the distribution of the number of directional samples used in the SAD analysis. The number of pixels

ACPD
15, 31665–31703, 2015

is increased in the scattering angle range of 60 to 160° and is decreased in the scattering angle range of 160 to 180°. There is a changing peak of the number of sample pixels in the scattering angle range of 140 to 160°. Figure 2b indicates the variation of the number of pixels with the different latitude. The number of pixels is changing significantly as a function of latitude and is lowest when the latitude is around 90° N and 90° S. C.-Labonnote et al. (2000) and Baran et al. (2006) proposed the SAD method for testing the phase function of the various ice particle models using POLDER observational data with multi-viewing angles. For investigating the phase functions (P_{11}) of the different ice crystal models for retrieving the cloud microphysical properties, the cloud spherical albedo as a function of scattering angle is required. For calculating the cloud spherical albedo, bi-directional reflection is first determined by:

$$R_{\mathrm{cld}}(\tau, r_{\mathrm{e}}, \omega, P_{11}; \mu, \mu_0, \phi - \phi_0) = \pi L_{\mathrm{obs}}(\mu\mu_0\phi - \phi_0)/\mu_0 F_0 \quad (3)$$

where τ, r_{e} and ω are the cloud optical thickness, effective cloud particle radius and bulk-scattering albedo, respectively; u, and u_0 are cosines of the satellite and solar zenith angles, respectively; ϕ is the relative azimuth angle between satellite and the sun; L_{obs} is the reflected solar radiance observed by satellite; F_0 is the solar flux density. Based on Eq. (3), τ and r_{e} can be retrieved from L_{obs} using a look-up table (LUT) method (Nakajima and King, 1990; Nakajima and Nakajima, 1995). Based on the retrievals of τ, R_{cld} is calculated by a radiative transfer model. Cloud plane albedo (A_{p}), spherical albedo (S) and are calculated by integrating over all the zenith and azimuth angles. The A_{p}, S and r_{e} are given as,

$$A_{\mathrm{p}}(\tau, r_{\mathrm{e}}; \mu_0) = \iint R_{\mathrm{cld}}(\mu, \mu_0, \phi - \phi_0)\mu d\mu d\phi \quad (4)$$

$$S(\tau r_{\mathrm{e}}) = \int A_{\mathrm{p}}(\mu_0)\mu_0 d\mu_0 \quad (5)$$

ACPD
15, 31665–31703, 2015

and

$$r_e = \int_0^{\infty} \tilde{r}^3 n(\tilde{r})\, d\tilde{r} \Big/ \int_0^{\infty} \tilde{r}^2 n(\tilde{r})\, d\tilde{r} \quad (6)$$

where $n(\tilde{r})$ is the number size distribution as a function of $\tilde{r}$. In Eq. (4), the values of R_{cld} over the range of viewing geometries is required for calculation of the cloud albedo. From that, cloud optical thickness is retrieved from L_{obs} data using the LUTs calculated from scattering property of various ice particle habits. Then, L_{obs} data over the range of satellite viewing geometries is simulated using a radiative transfer model. Based on these calculations, R_{cld} is calculated using Eq. (3).

Number of the cloud spherical albedo ($S(\theta)$) can be calculated from the L_{obs} in each pixel of the POLDER measurements with various scattering angles (θ) to investigate the P_{11} element of the ice particle models. Total observation number (N) of the L_{obs}, with various θ, is up to 16, which is limited to the viewing geometries of the measurements. Baran et al. (2006) assumed that if the scattering phase function of the ice particle model is correct, retrievals of the $\tau(\theta)$ and $S(\theta)$ in each direction should be the same and the SAD, as shown in Eq. (8), should be 0. $\bar{S}$, SAD and θ are given as,

$$\bar{S} = (1/N) \sum S(\theta) \quad (7)$$

$$\mathrm{SAD} = S(\theta) - \bar{S} \quad (8)$$

$$\cos\theta = \cos(\pi - u_0)\cos u + \sin u_0 \sin u \cos(\phi - \phi_0) \quad (9)$$

where u_0 and u are the solar and satellite zenith angles, respectively.

The steps to apply the SAD analysis to POLDER-3 measurements are as follows:

1. Calculate spherical albedo from the POLDER-3 measurements with 16 viewing geometries for each of the ice particle models.

ACPD
15, 31665–31703, 2015

2. Perform the SAD analysis by taking the difference between the directional and the direction-averaged cloud spherical albedo.

3. Assume that the phase function for each ice particle model adequately represents the phase function for all the ice particles in each pixel of the satellite measurement, and that the retrievals of the optical thickness and spherical albedo from the POLDER measurements with different viewing geometries are the same.

When SAD is 0, the mean spherical albedo and the spherical albedo from the specific angle of POLDER-3 measurements are the same. Therefore, the criteria for selecting the optimal particle habit of the ice cloud are defined as a SAD near 0 in the 16 viewing geometries of POLDER-3, and a small angular dependence.

4 Results and discussion

4.1 Characteristics of the single-scattering properties

To confirm the accuracy of the calculated single-scattering properties, the phase functions computed in this study are compared with other results. Figure 3 shows comparisons of the phase function (P_{11}) of hexagonal and spheroid particles calculated from the FDTD method with those derived from the ADDA (Bi et al., 2011) and **T**-matrix methods, respectively. Our FDTD results are the same as those calculated with the other methods. In addition, Ishimoto et al. (2012b) and Masuda et al. (2012) verify that the phase functions of ice particles with medium and large size parameters are the same by comparing the GOIE and GOM results, respectively.

Phase functions of the column, droxtal, plate, bullet-rosette, and Voronoi habit with various size parameters at wavelengths of 0.686 µm are given in Fig. 4. The phase functions depend on the particle habit and size parameters. There is a halo peak for the column, plate and bullet-rosette habit when the size parameter is larger than 100, as particle roughening is not applied in these calculations. For the droxtal, variation of

ACPD
15, 31665–31703, 2015

the phase function is evident when the size parameter is sufficiently small (SZP < 10). The POLDER-3 measures intensity from 16 viewing directions at scattering angles between 60–180°; for these scattering angles, the phase function curves of the various particles are different. The phase function of the Voronoi habit is very smooth, with features similar to those for severely roughened ice particle models and the IHM model except for the halo peak region as reported by Yang et al. (2013) and Doutriaux et al. (2000).

The asymmetry factor, single-scattering albedo, and extinction efficiency are some of the key parameters of the single-scattering properties of ice particles. Figure 5 shows the single-scattering properties of various ice particle habits at the wavelengths of 1.05 and 2.2 µm for various size parameters. The extinction efficiency increases with the size parameter up to approximately 10 and converges gradually to 2 when the size parameter is larger than 100. The maximum values of the extinction efficiency appear when the size parameter is around 10. However, the location of the maximum extinction efficiency varies with particle habit. There is a smooth peak in the asymmetry factor for the size parameter from 1 to 10. The peak of the asymmetry factor at a wavelength of 2.1 µm is larger than that at 1.05 µm.

Figure 6 shows the comparison of the satellite-observed radiance from the column ice particle model with the other four models at wavelengths of 1.05 and 2.21 µm as a function of optical thickness τ and effective cloud particle radius r_e. The radiance is calculated from the RSTAR radiative transfer model (Nakajima and Tanaka, 1986; Sekiguchi and Nakajima, 2008), which is a general package for simulating radiation fields in the atmosphere-land-ocean system at wavelengths between 0.17 and 1000 µm. The solar zenith, viewing zenith, and relative azimuth angles are 40, 30, and 90°, respectively. The satellite-observed radiance at a wavelength of 2.21 µm for the column habit is similar to the plate and droxtal models for the same r_e but different at the 1.05 µm wavelength. The radiances from the column model are significantly different from those obtained with the bullet-rosette and Voronoi models, which results in different values of the inferred τ and r_e. Thus, the determination of the effective ice par-

ACPD
15, 31665–31703, 2015

ticle model is important for reducing the retrieval error caused by using different particle models.

4.2 SAD analysis

Figure 7 shows the SAD analysis as a function of the scattering angle, effective particle radius, and ice particle model. The SAD of the droxtal, column and plate show substantial variations in both the scattering angle and effective particle radius. The variation of SAD for the bullet-rosette model is more smoothly distributed close to 0 value of the SAD (hereafter, "zero line") than with the droxtal, plate, and column models for small ($6 < \tilde{r} < 10\,\mu m$), medium ($28 < \tilde{r} < 38\,\mu m$), and large particles ($70 < \tilde{r} < 100\,\mu m$). However, the SAD peak of the bullet-rosette model varies in the scattering angle range of 140 to 160° with medium and large particles. The SAD of the Voronoi model is closest to the zero line over the entire scattering angle range for small, medium and large particles. Both the Voronoi and bullet-rosette model with small particles are smoothly distributed along the zero line.

Figure 8 shows the slope of the regression function (SRF) and total relative albedo difference (TRAD) of the SAD for the same five ice particle models with small, medium and large particles as shown in Fig. 7. Both values of the SRF and TRAD for small particles of the bullet-rosette, for medium and large particles of the bullet-rosette and Voronoi models, are smallest of all the single particle models considered. However, there is a changing peak of the SAD in the scattering angle range of 140 to 160° for bullet-rosette model with medium and large particles. The SRF for large particles and TRAD for all size of particles with droxtal model are largest in the all ice particle models. As we have described in Sect. 3, the effective particle habit is defined as a smallest value of the SRF and TRAD. Thus, it was confirmed that the bullet-rosette model with small particles and Voronoi model with medium and large particles are sufficiently accurate for the retrieval of the ice cloud spherical albedo and optical thickness. Thus, these models are sufficient to represent cirrus in terms of effective habit models for the purposes of the SGLI sensor.

ACPD
15, 31665–31703, 2015

Ice crystals in ice cloud are complex. To simulate this complexity, we assume different values of distortion (as defined by Macke et al., 1996) and apply these to the ensemble model. Numerous previous studies have shown that the degree of distortion is an important property to consider when retrieving ice cloud optical properties from multiple-view instruments. To investigate the influence of the distortion of the ice particle model on retrieval of the ice cloud property, we performed the SAD analysis using the ensemble ice particle models with $\widetilde{r} = 30\,\mu m$, assuming a number of distortion values (see Fig. 9). The variation of SAD for the no distortion model in Fig. 9a is largest relative to the other distortion values. As a function of distortion value, there are significant variations in the SAD analysis in the scattering angle range of 60 to 80° and 140 to 160°. There is no obvious difference of the SAD between Fig. 9b, Fig. 9c and Fig. 9d for various degrees of the distortions. The SAD of the ice particle models with a distortion values of 0.4 with spherical air bubbles in Fig. 9e is closest to the zero line. It is implied that the models with distortion or surface roughness are best for the retrieval of the ice cloud optical property than with no distortion applied to the model. The model with spherical air bubbles and distortion is most efficient than the models with distortion only.

Several conventional studies demonstrated that ice particle models such as ensemble ice particle model, IHM and GHM and some aggregated complex models, with rough surface are useful for the operational satellite data processing (C.-Labonnote et al., 2000, 2001; Doutriaux et al., 2000; Baum et al., 2011, 2014; Baran and Labnnote,. 2006, 2007 and Cole et al., 2013). For evaluating the accuracy of the Voronoi model, we further compared the SAD of the Voronoi model with the conventional IHM, GHM, 5-plate aggregate and ensemble ice particle models with $\widetilde{r} = 30\,\mu m$. As shown in Fig. 10, all of the selected models do not have any strong angular dependence. However, all the models in Fig. 10 have a rough surface except for the IHM containing spherical air bubbles and Voronoi habit. It is implied that the Voronoi habit model has a similar effect as some aggregated and mixed-habit ice particle models with roughened surfaces

ACPD
15, 31665–31703, 2015

and the IHM single particle model containing air bubbles on retrieval of the ice cloud properties using remote sensing instruments.

Figure 11 shows the slope of the regression function (top panel) and total relative albedo difference (bottom panel) for the selected models in Fig. 10. The SRF for ensemble ice particle model, GHM and Voronoi model was significantly smaller than the other two models. The TRAD for all of the habit models is not significantly different from each other. However, Voronoi model is little bit smaller than the other models except for ensemble ice particle model. Voronoi model has both of the small values of SRF and TRAD, which is similar to ensemble ice particle model, indicating that SAD of the Voronoi model has a low angular dependence.

5 Conclusions

Ice particle single-scattering properties are investigated for potential use in the GCOM-C satellite program. The single-scattering properties of five different ice particle models (plates, columns, droxtals, bullet-rosettes, and Voronoi) are developed using the FDTD, GOIE and GOM methods. The accuracy of the single-scattering property is investigated by comparing the phase function from the FDTD method used in this study to conventional results from ADDA and **T**-matrix method. The FDTD phase functions are also compared with computational results from GOIE. Results indicate that the FDTD-based phase functions are consistent with results from the ADDA, **T**-matrix and GOIE methods and suggest that the single-scattering property database developed in this study is reliable for use in radiative transfer simulations and applications in the remote sensing of ice cloud.

The characteristics of the single-scattering property database are investigated by analyzing the asymmetry factor, single-scattering albedo, and extinction efficiency. Each of the five habits are employed to compare top-of-atmosphere radiances as a function of the optical thickness and effective particle radius. Results indicate that the satellite-observed radiances from the column model are significantly different from those ob-

ACPD
15, 31665–31703, 2015

tained with the bullet-rosette and Voronoi models when the effective particle radius is larger than 8. These results imply that the choice of ice particle habit is important for reducing the retrieval error.

Furthermore, the SAD analysis is performed to determine the optimal ice particle habit for retrieving the optical thickness and cloud spherical albedo using POLDER-3 multi-angle measurements. Retrievals are performed using 589 246 pixels of the POLDER-3 observation data with a global scale over ocean from days 20–22 March, June, September, and December 2003. The following conclusions are drawn from these results.

The SADs of the droxtal and column habits show significant variations with scattering angle and effective particle radius.

The variation of the SAD for small particles with bullet-rosette model is more smoothly distributed along the zero line than other habit models.

The SAD of the Voronoi model is closest to the zero line with scattering angle for all size of particles.

The bullet-rosette habit for small particles and Voronoi habit for all size of particles are most suitable for retrieving the ice cloud spherical albedo and optical thickness.

The results of the SAD analysis from the Voronoi model are compared with the result from the conventional IHM, GHM, 5-plate aggregate and ensemble ice particle model with moderate ice particle size for evaluating the efficiency of the Voronoi model on retrieving ice clouds optical properties. It is concluded that the Voronoi habit model is similar to the conventional efficient models for retrieval of the ice cloud properties using remote sensing instruments. The results of this study are not only useful for developing the ice cloud products of the GCOM-C/SGLI satellite mission, but also useful for determining the optimal ice particle habit for ice cloud remote sensing.

Acknowledgements. This work was supported by the GCOM-C/SGLI and EarthCARE project of the Japan Aerospace Exploration Agency (JAXA), and the Japan Science and Technology Agency (JST), CREST/EMS/TEEDDA. The authors would like to thanks ICARE and CNES for providing the POLDER data as well as François Thieuleux for his support with POLDER data

ACPD
15, 31665–31703, 2015

analysis. The authors gratefully acknowledge Bryan A. Baum (UW-Madison) for providing the GHM ice particle model.

References

Baran, A. J. and C.-Labonnote, L.: On the reflection and polarization properties of ice cloud, J. Quant. Spectrosc. Ra., 100, 41–54, 2006.

Baran, A. J. and C.-Labonnote, L.: A ensemble ice particle scattering model for cirrus, I: The solar region, Q. J. Roy. Meteor. Soc., 133, 1899–1912, 2007.

Baran, A. J., Watts, P. D., and Foot, J. S.: Potential retrieval of dominating crystal habit and size using radiance data from a dual-view and multiwavelength instrument: A tropical cirrus anvil case, J. Geophys. Res., 103, 6075–6082, 1998.

Baran, A. J., Watts, P. D., and Francis, P. N.: Testing the coherence of cirrus microphysical and bulk properties retrieved from dual-viewing multispectral satellite radiance measurements. J. Geophys. Res., 104, 31673–31683, 1999.

Baran A. J., Francis, P. N., Labonnote, L. C., and Doutriaux-Boucher, M.: A scattering phase function for ice cloud: Tests of applicability using aircraft and satellite multi-angle multiwavelength radiance measurements of cirrus, Q. J. Roy. Meteorol. Soc., 127, 2395–2416, 2001.

Baran, A. J., Havemann, S, Francis, P. N., and Watts, P. D.: A consistent set of single-scattering properties for cirrus cloud: tests using radiance measurements from a dual-viewing multi-wavelength satellite-based instrument, J. Quant. Spectrosc. Radiat. Transfer, 79–80, 549–67, 2003.

Baran, A. J., Hill, P., Furtado, K., Field, P., and Manners, J.: A Coupled Cloud Physics–Radiation Parameterization of the Bulk Optical Properties of Cirrus and Its Impact on the Met Office Unified Model Global Atmosphere 5.0 Configuration, J. Climate, 27, 7725–7752, 2014.

Baran, A. J., Furtado, K., Labonnote, L.-C., Havemann, S., Thelen, J.-C., and Marenco, F.: On the relationship between the scattering phase function of cirrus and the atmospheric state, Atmos. Chem. Phys., 15, 1105–1127, doi:10.5194/acp-15-1105-2015, 2015.

Baum, B. A., Yang, P., Heymsfield, A. J., Platnick, S., King, M. D., and Bedka, S. T.: Bulk scattering models for the remote sensing of ice clouds. Part 2: Narrowband models, J. Appl. Meteorol., 44, 1896–1911, 2005.

ACPD
15, 31665–31703, 2015

Baum, B. A., Yang, P., Heymsfield, A. J., Schmitt, C., Xie, Y., Bansemer, A., Hu, Y.-X., and Zhang, Z.: Improvements to shortwave bulk scattering and absorption models for the remote sensing of ice clouds, J. Appl. Meteorol. Clim., 50, 1037–1056, 2011.

Baum, B. A., Yang, P., Heymsfield, A. J., Bansemer, A., Cole, B. H., Merrelli, A., Schmitt, C., and Wang, C.: Ice cloud single-scattering property models with the full phase matrix at wavelengths from 0.2 to 100 µm, J. Quant. Spectrosc. Radiat. Transfer, 146, 123–139, 2014.

Bi, L., Yang, P., and Kattawar, G. W.: Edge-effect contribution to the extinction of light by dielectric disk and cylindrical particles, Appl. Opt., 49, 4641–4646, 2010.

Bi, L., Yang, P., Kattawar, G. W., Hu, Y., and Baum, B. A.: Scattering and absorption of light by ice particles: solution by a new physical-geometric optics hybrid method, J. Quant. Spectrosc. Radiat. Transfer., 112, 1492–1508, 2011.

Bi, L. and Yang, P.: High-frequency extinction efficiencies of spheroids: rigorous **T**-matrix solutions and semi-empirical approximations, Optics Express, 22, 10270–10293, 2014.

Bi, L. and Yang, P.: Accurate simulation of the optical properties of atmospheric ice crystals with invariant imbedding **T**-matrix method, J. Quant. Spectrosc. Radiat. Transfer, 138, 17–35, 2014.

Chen, G., Yang, P., and Kattawar, G. W.: Application of the pseudospectral time-domain method to the scattering of light by nonspherical particles, J. Opt. Soc. Am. A, 25, 785–790, 2008.

Chepfer, H., Brogniez, G., and Fouquart, Y.: Cirrus clouds' mi- crophysical properties deduced from POLDER observations, J. Quant. Spectrosc. Radiat. Transfer, 60, 375–390, 1998.

Chepfer, H., Goloub, P., Riedi, J., de Haan, J. F., and Hovenier, J. W.: Ice crystal shapes in cirrus clouds derived from POLDER-1/ADEOS-1, J. Geophys. Res., 106, 7955–7966, doi:10.1029/2000JD900285, 2001.

Chepfer, H., Minnis, P., Young, D., Nguyen, L., and Arduini, R. F.: Estimation of cirrus cloud effective ice crystal shapes using visible reflectances from dual-satellite measurements, J. Geophys. Res., 107, 4730, doi:10.1029/2000JD000240, 2002.

Cole, B., Yang, P., Baum, B. A., Riedi, J., C.-Labonnote, L., Thieuleux, F., and Platnick, S.: Comparison of PARASOL observations with polarized reflectances simulated using different ice habit mixtures, J. Appl. Meteor. Clim., 52, 186–196, 2013.

Cole, B. H., Yang, P., Baum, B. A., Riedi, J., and C.-Labonnote, L.: Ice particle habit and surface roughness derived from PARASOL polarization measurements, Atmos. Chem. Phys., 14, 3739–3750, doi:10.5194/acp-14-3739-2014, 2014.

ACPD
15, 31665–31703, 2015

Doutriaux-Boucher, M., Buriez, J. C., Brogniez, G., Labonnote, L. C., and Baran, A. J.: Sensitivity of retrieved POLDER directional cloud optical thickness to various ice particle models. Geophys. Res. Lett., 27, 109–112, 2000.

Draine, B. T. and Flatau, P. J.: Discrete-dipole approximation for scattering calculations, J. Opt. Soc. Am. A, 11, 1491–1499, 1994.

Foot, J. S.: Some observations of the optical properties of clouds. II: Cirrus, Q. J. Roy. Meteorol. Soc., 114, 145–164, 1988.

Forster, P., Ramaswamy, V., Artaxo, P., Berntsen, T., Betts, R., Fahey, D., Haywood, J., Lean, J., Lowe, D., Myhre, G., Nganga, J., Prinn, R., Raga, G., Schulz, M., and Van Dorland, R.: Changes in Atmospheric Constituents and in Radiative Forcing, in: IPCC Fourth Assessment Report WG 1, edited by: Solomon, S., Qin, D., Manning, M., Chen, Z., Marquis, M., Averyt, K. B., Tignor, M., and Miller, H. L., Cambridge University Press, Cambridge, UK, 129–234, 2007.

Hess, M. and Wiegner, M.: COP: A data library of optical properties of hexagonal ice crystals, Appl. Opt., 33, 7740–7746, 1994.

Heymsfield, A. J.: Properties of Tropical and Midlatitude Ice Cloud Particle Ensembles. Part I: Median Mass Diameters and Terminal Velocities, J. Atmos. Sci., 60, 2573–2591, 2003.

Heymsfield, A. J., Bansemer, A., Field, P. R., Durden, S. L., Stith, J. L., Dye, J. E., Hall, W., and Grainger, C. A.: Observations and Parameterizations of Particle Size Distributions in Deep Tropical Cirrus and Stratiform Precipitating Clouds: Results from In Situ Observations in TRMM Field Campaigns, J. Atmos. Sci., 59, 3457–3491, 2002.

Imaoka, K., Kachi, M., Fujii, H., Murakami, H., Hori, M., Ono, A., and Shimoda, H.: Global Change Observation Mission (GCOM) for monitoring carbon, water cycles, and climate change, Proc IEEE, 98, 717–734, 2010.

Ishimoto, H., Masuda, K., Mano, Y., Orikasa, N., and Uchiyama, A.: Optical modeling of irregularly shaped ice particles in convective cirrus, in: radiation processed in the atmosphere and ocean (IRS2012): Proceedings of the International Radiation Symposium (IRC/IAMAS) 1531, 184–187, 2012a.

Ishimoto, H., Masuda, K., Mano, Y., Orikasa, N., and Uchiyama, A.: Irregularly shaped ice aggregates in optical modeling of convectively generated ice clouds, J. Quant. Spectrosc. Radiat. Transfer, 113, 632–643, 2012b.

ACPD
15, 31665–31703, 2015

Knap, W. H., C.-Labonnote, L., Brogniez, G., and Stammes, P.: Modeling total and polarized reflectances of ice clouds: Evaluation by means of POLDER and ATSR-2 measure- ments, Appl. Opt., 44, 4060–4073, 2005.

C.-Labonnote, L., Brogniez, G., Doutriaux-Boucher, M., Buriez, J. C., Gayet, J. F., and Chepfer, H.: Modeling of light scattering in cirrus clouds with inhomogeneous hexagonal monocrystals. Comparison with in-situ and ADEOS-POLDER measurements, Geophys. Res. Lett., 27, 113–116, 2000.

C.-Labonnote, L., Brogniez, G., Buriez, J. C., and Doutriaux-Boucher, M.: Polarized light scattering by inhomogeneous hexagonal monocrystals: validation with ADEOS-POLDER measurements, J. Geophys. Res., 106, 12139–12153, 2001.

Letu, H., Nakajima, T. Y., and Matsui, T. N.: Development of an ice crystal scattering database for the global change observation mission/second generation global imager satellite mission: Investigating the refractive index grid system and potential retrieval error, Appl. Opt., 51, 6172–6178, 2012.

Liou, K. N.: Influence of Cirrus Clouds on Weather and Climate Processes: A Global Perspective, Mon. Weather Rev., 114, 1167–1199, 1986.

Liu, Q. H.: The PSTD algorithm: a time-domain method requiring only two cells per wavelength, Microwave Opt. Technol. Lett., 15, 158–165, 1997.

Liu, Q. H.: The pseudospectral time-domain (PSTD) algorithm for acoustic waves in absorptive media, IEEE Trans. Ultrason. Ferroelectr. Freq. Control, 45, 1044–1055, 1998.

Liu, C., Panetta, R. L., and Yang, P.: Application of the pseudo-spectral time domain method to compute particle single-scattering properties for size parameters up to 200, J. Quant. Spectrosc. Radiat. Transfer, 113, 1728–1740, 2012.

Liu, C., Yang, P., Minnis, P., Loeb, N., Kato, S., Heymsfield, A., and Schmitt, C.: A two-habit model for the microphysical and optical properties of ice clouds, Atmos. Chem. Phys., 14, 13719–13737, doi:10.5194/acp-14-13719-2014, 2014.

Macke, A.: Scattering of light by polyhedral ice crystals, Appl. Opt., 32, 2780–2788, 1993.

Macke, A., Mishchenko, M. I., and Cairns, B.: The influence of inclusions on light scattering by large ice particles, J. Geophys. Res., 101, 23311–23316, 1996a.

Macke, A., Mueller, J., and Raschke, E.: Single Scattering Properties of Atmospheric Ice Crystals, J. Atmos. Sci., 53, 2813–2825, 1996b.

ACPD
15, 31665–31703, 2015

Masuda, K., Ishimoto, H., and Takashima, T.: Retrieval of cirrus optical thickness and ice-shape information using total and polarized reflectance from satellite measurements, J. Quant. Spectrosc. Radiat. Transfer, 75, 39–51, 2002.
Masuda, K., Ishimoto, H., and Mano, Y.: Efficient method of computing a geometric optics integral for light scattering, Meteorol. Geophys., 63, 15–19, 2012.
McFarquhar, G. M. and Heymsfield, A. J.: Microphysical characteristics of three anvils sampled during the Central Equatorial Pacific Experiment, J. Atmos. Sci., 53, 2401–2423, 1996.
Nakajima, T. and King, M. D.: Determination of the optical thickness and effective particle radius of clouds from reflected solar radiation measurements. Part I: Theory, J. Atmos. Sci., 47, 1878–1893, 1990.
Nakajima, T. Y and Nakajima, T.: Wide-area determination of cloud microphysical properties from NOAA AVHRR measure- ments for FIRE and ASTEX regions, J. Atmos. Sci., 52, 4043–4059, 1995.
Nakajima, T. and Tanaka, M.: Matrix formulations for the transfer of solar radiation in a plane-parallel scattering atmosphere, J. Quant. Spectrosc. Radiat. Transfer, 35, 13–21, 1986.
Nakajima, T. Y., Nakajima, T., Yoshimori, K., Mishra, S. K., and Tripathi, S. N.: Development of a light scattering solver applicable to particles of arbitrary shape on the basis of the surface integral equations method of Muller-type (SIEM/M): Part I. Methodology, accuracy of calculation, and electromagnetic current on the particle surface, Appl. Opt., 48, 3526–3536, 2009.
Nakajima, T. Y., Tsuchiya, T., Ishida, H., Matsui, T. N., and Shimoda, H.: Cloud detection performance of spaceborne visible-to-infrared multispectral imagers, Appl. Opt., 50, 2601–2616, 2011.
Nousiainen, T., Lindqvist, H., McFarquhar, G. M., and Um, J.: Small irregular ice crystals in tropical cirrus, J. Atmos. Sci., 68, 2614–2627, doi:10.1175/2011JAS3733.1, 2011.
Ohser, J. and Mücklich, F.: Statistical analysis of microstructures in materials science, Chichester: Wiley, 2000.
Ottaviani, M., Cairns, B., Chowdhary, J., van Diedenhoven, B., Knobelspiesse, K., Hostetler, C., Ferrare, R., Burton, S., Hair, J., Obland, M., and Rogers, R.: Polarimetric retrievals of surface and cirrus clouds properties in the region affected by the deep-water horizon oil spill, Remote Sens. Environ., 121, 389–403, doi:10.1016/j.rse.2012.02.016, 2012.
Purcell, E. M. and Pennypacker, C. R.: Scattering and absorption of light by nonspherical dielectric grains, The Astrophysical Journal, 186, 705–714, 1973.

ACPD
15, 31665–31703, 2015

Sekiguchi, M. and Nakajima, T.: A k-distribution-based radiation code and its computational optimization for an atmospheric general circulation model, J. Quant. Spectrosc. Radiat. Transfer, 109, 2779–2793, 2008.
Sun, W., Fu, Q., and Chen, Z.: Finite-difference time-domain solution of light scattering by dielectric particles with perfectly matched layer absorbing boundary conditions, Appl. Opt., 38, 3141–3151, 1999.
Sun, W., Loeb, N., and Yang, P.: On the retrieval of ice cloud particle shapes from POLDER measurements, J. Quant. Spectrosc. Radiat. Transfer, 101, 435–447, 2006.
Takano, Y. and Liou, K. N.: Solar radiative transfer in cirrus clouds. Part I. Single-scattering and optical properties of hexagonal ice crystals, J. Atmos. Sci., 46, 3–19, 1989.
Takano, Y. and Liou, K. N.: Transfer of polarized infrared radiation in optically anisotropic media: application to horizontally oriented ice crystals, J. Opt. Soc. Am. A, 10, 1243–1256, 1993.
Um, J. and McFarquhar, G. M.: Single-scattering properties of aggregates of bullet rosettes in cirrus, J. Appl. Meteorol. Clim., 46, 757–775, doi:10.1175/JAM2501.1, 2007.
Um, J. and McFarquhar, G. M.: Single-scattering properties of aggregates of plates, Q. J. Roy. Meteorol. Soc., 135, 291–304, doi:10.1002/qj.378, 2009.
Um, J. and McFarquhar, G. M.: Dependence of the single-scattering properties of small ice crystals on idealized shape models, Atmos. Chem. Phys., 11, 3159–3171, doi:10.5194/acp-11-3159-2011, 2011.
van Diedenhoven, B., Cairns, B., Geogdzhayev, I. V., Fridlind, A. M., Ackerman, A. S., Yang, P., and Baum, B. A.: Remote sensing of ice crystal asymmetry parameter using multi-directional polarization measurements – Part 1: Methodology and evaluation with simulated measurements, Atmos. Meas. Tech., 5, 2361–2374, doi:10.5194/amt-5-2361-2012, 2012.
Van Diedenhoven, B., Fridlind, A. M., Cairns, B., and Ackerman, A. S.: Variation of ice crystal size, shape and asymmetry parameter in tops of tropical deep convective clouds, J. Geophys. Res.-Atmos., 119, 11809–11825, 2014.
Warren, S. G. and Brandt, R. E.: Optical constants of ice from the ultraviolet to the microwave: A revised compilation, J. Geophys. Res. (1984–2012), 113, doi:10.1029/2007JD009744, 2008.
Yang, P. and Liou, K. N.: Geometric-optics – integral-equation method for light scattering by nonspherical ice crystals, Appl. Opt., 35, 6568–6584, 1996.
Yang, P. and Liou, K. N.: An efficient algorithm for truncating spatial domain in modeling light scattering by finite-difference technique, J. Comput. Phys., 140, 346–369, 1998a.

ACPD
15, 31665–31703, 2015

Yang, P. and Liou, K. N.: Single-scattering properties of complex ice crystals in terrestrial atmosphere, Contrib. Atmos. Phys., 71, 223–248, 1998b.
Yang, P., Liou, K. N., Wyser, K., and Mitchell, D.: Parameterization of the scattering and absorption properties of individual ice crystals, J. Geophys. Res., 105, 4699–4718, 2000.
Yang, P., Wei, H., Huang, H.-L., Baum, B. A., Hu, Y. X., Kattawar, G. W., Mishchenko, M. I., and Fu, Q.: Scattering and absorption property database for nonspherical ice particles in the near- through far-infrared spectral region, Appl. Opt., 44, 5512–5523, 2005.
Yang, P., Bi, L., Baum, B. A., Liou, K. N., Kattawar, G. W., Mishchenko, M. I., and Cole, B.: Spectrally consistent scattering, absorption, and polarization properties of atmospheric ice crystals at wavelengths from 02 to 100 µm, J. Atmos. Sci., 70, 330–347, 2013.
Yang, P., Liou, K. N., Bi, L., Liu, C., Yi, B. Q., and Baum, B. A.: On the radiative properties of ice clouds: Light scattering, remote sensing, and radiation parameterization, Adv. Atmos. Sci., 32, 32–63, 2015.
Yee, S. K.: Numerical solution of initial boundary value problems involving Maxwell's equations in isotropic media, IEEE Trans. Antennas Propag., 14, 302–307, 1966.
Yi, B., Yang, P., Baum, B. A., L'Ecuyer, T., Oreopoulos, L., Mlawer, E. J., Heymsfield, A. J., and Liou, K. N.: Influence of ice particle surface roughening on global cloud radiative effect, J. Atmos. Sci., 70, 2794–2807, 2013.
Yurkin, M. A., Maltsev, V. P., and Hoekstra, A. G.: The discrete dipole approximation for simulation of light scattering by particles much larger than the wavelength, J. Quant. Spectrosc. Radiat. Transfer., 106, 546–557, 2007.
Zhang, Z., Yang, P., Kattawar, G., Riedi, J., C.-Labonnote, L. C., Baum, B. A., Platnick, S., and Huang, H.-L.: Influence of ice particle model on satellite ice cloud retrieval: lessons learned from MODIS and POLDER cloud product comparison, Atmos. Chem. Phys., 9, 7115–7129, doi:10.5194/acp-9-7115-2009, 2009.

ACPD
15, 31665–31703, 2015

Table 1. Specification of the SGLI.

No.	SGLI Channels	Center Wavelength (μm)	Band width (nm)	IFOV (m)
1	VN1	0.380	10	250
2	VN2	0.412	10	250
3	NV3	0.443	10	250
4	NV4	0.490	10	250
5	NV5	0.530	20	250
6	NV6	0.565	20	250
7	NV7	0.673	20	250
8	NV8	0.673	20	250
9	NV9	0.763	12	1000
10	NV10	0.868	20	250
11	NV11	0.868	20	250
12	P1	0.673	20	1000
13	P2	0.868	20	1000
14	SW1	1.050	20	1000
15	SW2	1.380	20	1000
16	SW3	1.630	200	250
17	SW4	2.210	50	1000
18	T1	10.8	740	500
19	T2	12.0	740	500

ACPD
15, 31665–31703, 2015

Table 2. Size parameter with various particle size and calculating wavelength on the SGLI channels (FDTD, GOIE, GOM).

λ (μm)	$\tilde{r}$ (μm)								
	0.5500	0.5650	0.5800	0.6590	0.6740	0.6860	0.8530	0.8650	0.8830
0.700	7.997	7.784	7.583	6.674	6.526	6.411	5.156	5.085	4.981
1.000	11.424	11.121	10.833	9.534	9.322	9.159	7.366	7.264	7.116
1.300	14.851	14.457	14.083	12.395	12.119	11.907	9.576	9.443	9.250
1.900	21.706	21.129	20.583	18.115	17.712	17.402	13.995	13.801	13.520
2.600	29.702	28.914	28.166	24.790	24.238	23.814	19.152	18.886	18.501
3.500	39.984	38.922	37.916	33.370	32.628	32.057	25.781	25.423	24.905
4.900	55.977	54.491	53.082	46.719	45.679	44.880	36.093	35.593	34.867
6.900	78.825	76.733	74.748	65.788	64.323	63.198	50.825	50.120	49.099
9.500	108.528	105.646	102.914	90.577	88.561	87.012	69.977	69.006	67.599
13.200	150.796	146.793	142.997	125.854	123.053	120.901	97.231	95.882	93.928
18.200	207.916	202.396	197.162	173.527	169.665	166.697	134.061	132.201	129.506
25.300	289.027	281.353	274.077	241.221	235.853	231.727	186.359	183.774	180.028
35.100	400.981	390.336	380.241	334.658	327.210	321.487	258.546	254.959	249.762
47.300	540.354	5307.901	5170.628	4550.780	4449.502	4371.668	3515.785	3467.011	3396.336
60.600	692.293	673.913	656.485	577.786	564.927	555.045	446.379	440.186	431.213
77.100	880.788	857.405	835.230	735.104	718.744	706.171	567.917	560.039	548.622
97.500	1113.837	1084.266	1056.225	929.606	908.918	893.018	718.184	708.220	693.783
122.800	1402.864	1365.620	1330.302	1170.827	1144.770	1124.745	904.543	891.994	873.811
154.000	1759.292	1712.585	1668.294	1468.301	1435.624	1410.511	1134.362	1118.625	1095.822
2201.400	2142.955	2087.534	1837.283	1796.394	1764.971	1419.425	1399.734	1371.200	
242.300	2768.029	2694.541	2624.855	2310.191	2258.777	2219.265	1784.778	1760.018	1724.140
308.400	3523.153	3429.618	3340.921	2940.416	2874.977	2824.686	2271.670	2240.155	2194.490
416.380	4756.714	4630.430	4510.677	3969.943	3881.592	3813.692	3067.049	3024.500	2962.846
533.800	6098.117	5936.220	5782.697	5089.475	4976.208	4889.161	3931.963	3877.415	3798.374

ACPD
15, 31665–31703, 2015

Table 2. Continued.

λ (μm)	$\tilde{r}$ (μm)								
	1.0350	1.0500	1.0650	1.3650	1.3800	1.3950	1.4800	1.6300	1.7800
0.700	4.249	4.189	4.130	3.222	3.187	3.153	2.972	2.698	2.471
1.000	6.071	5.984	5.900	4.603	4.553	4.504	4.245	3.855	3.530
1.300	7.892	7.779	7.670	5.984	5.919	5.855	5.519	5.011	4.589
1.900	11.534	11.370	11.209	8.746	8.651	8.558	8.066	7.324	6.707
2.600	15.784	15.558	15.339	11.968	11.838	11.711	11.038	10.022	9.178
3.500	21.247	20.944	20.649	16.111	15.936	15.764	14.859	13.492	12.355
4.900	29.746	29.322	28.909	22.555	22.310	22.070	20.802	18.888	17.296
6.900	41.888	41.290	40.708	31.761	31.416	31.078	29.293	26.598	24.356
9.500	57.672	56.848	56.047	43.729	43.254	42.789	40.331	36.620	33.534
13.200	80.133	78.989	77.876	60.760	60.100	59.454	56.039	50.882	46.594
18.200	110.487	108.909	107.375	83.776	82.865	81.974	77.266	70.156	64.244
25.300	153.589	151.395	149.263	116.458	115.192	113.953	107.409	97.524	89.306
35.100	213.082	210.038	207.080	161.568	159.811	158.093	149.013	135.300	123.899
47.300	2897.550	2856.157	2815.929	2197.043	2173.163	2149.795	2026.327	1839.855	1684.811
60.600	367.885	362.630	357.522	278.946	275.914	272.947	257.271	233.596	213.911
77.100	468.052	461.365	454.867	354.896	351.039	347.264	327.320	297.199	272.154
97.500	591.894	583.439	575.221	448.799	443.921	439.147	413.926	375.835	344.163
122.800	745.483	734.833	724.484	565.257	559.112	553.100	521.335	473.359	433.469
154.000	934.889	921.534	908.554	708.872	701.167	693.628	653.791	593.626	543.601
192.700	1169.826	1153.114	1136.873	887.011	877.369	867.935	818.088	742.804	680.208
242.300	1470.933	1449.920	1429.498	1115.323	1103.200	1091.337	1028.659	933.997	855.290
308.400	1872.207	1845.461	1819.469	1419.586	1404.155	1389.057	1309.280	1188.794	1088.615
416.380	2527.722	2491.612	2456.519	1916.625	1895.792	1875.407	1767.698	1605.026	1469.771
533.800	3240.545	3194.252	3149.262	2457.117	2430.409	2404.275	2266.192	2057.647	1884.250

ACPD
15, 31665–31703, 2015

Table 2. Continued.

λ (μm)	$\tilde{r}$ (μm)								
2.1730	2.2100	2.2480	10.2450	10.8000	11.3550	11.4450	12.0000	12.5550	
0.700	2.024	1.990	1.957	0.429	0.407	0.387	0.384	0.367	0.350
1.000	2.891	2.843	2.795	0.613	0.582	0.553	0.549	0.524	0.500
1.300	3.759	3.696	3.634	0.797	0.756	0.719	0.714	0.681	0.651
1.900	5.494	5.402	5.311	1.165	1.105	1.051	1.043	0.995	0.951
2.600	7.518	7.392	7.267	1.595	1.513	1.439	1.427	1.361	1.301
3.500	10.120	9.951	9.783	2.147	2.036	1.937	1.921	1.833	1.752
4.900	14.168	13.931	13.696	3.005	2.851	2.711	2.690	2.566	2.452
6.900	19.951	19.617	19.286	4.232	4.014	3.818	3.788	3.613	3.453
9.500	27.469	27.009	26.553	5.826	5.527	5.257	5.215	4.974	4.754
13.200	38.168	37.529	36.894	8.095	7.679	7.304	7.247	6.912	6.606
18.200	52.625	51.744	50.869	11.162	10.588	10.071	9.992	9.529	9.108
25.300	73.154	71.930	70.714	15.516	14.719	14.000	13.889	13.247	12.661
35.100	101.491	99.792	98.105	21.527	20.420	19.422	19.270	18.378	17.566
47.300	1380.103	1356.997	1334.059	292.725	277.682	264.110	262.033	249.914	238.866
60.600	175.224	172.290	169.378	37.166	35.256	33.532	33.269	31.730	30.327
77.100	222.933	219.201	215.495	47.285	44.855	42.663	42.327	40.369	38.585
97.500	281.919	277.199	272.514	59.796	56.723	53.951	53.526	51.051	48.794
122.800	355.074	349.129	343.227	75.312	71.442	67.950	67.416	64.298	61.456
154.000	445.288	437.833	430.432	94.447	89.594	85.214	84.544	80.634	77.070
192.700	557.188	547.860	538.599	118.182	112.108	106.629	105.790	100.897	96.437
242.300	700.606	688.876	677.231	148.601	140.964	134.074	133.020	126.868	121.260
308.400	891.732	876.803	861.981	189.140	179.420	170.650	169.308	161.478	154.340
416.380	1203.954	1183.798	1163.787	255.363	242.240	230.400	228.588	218.016	208.379
533.800	1543.472	1517.631	1491.977	327.376	310.552	295.373	293.051	279.497	267.142

ACPD
15, 31665–31703, 2015

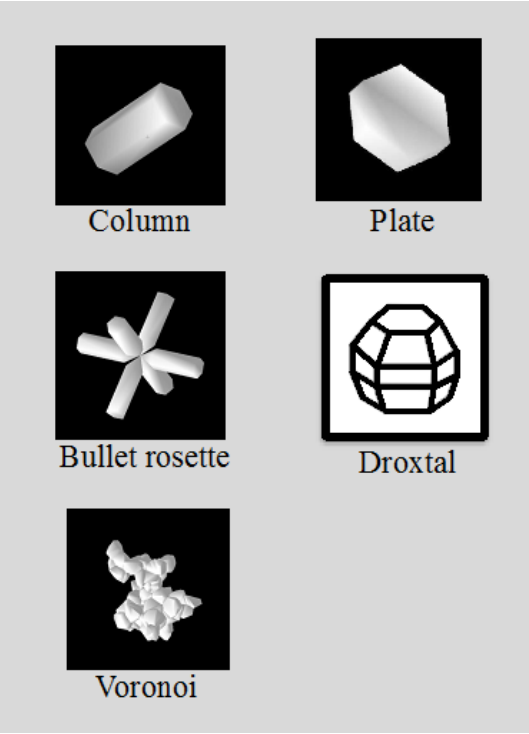

Figure 1. SGLI cloud particle habits.

ACPD
15, 31665–31703, 2015

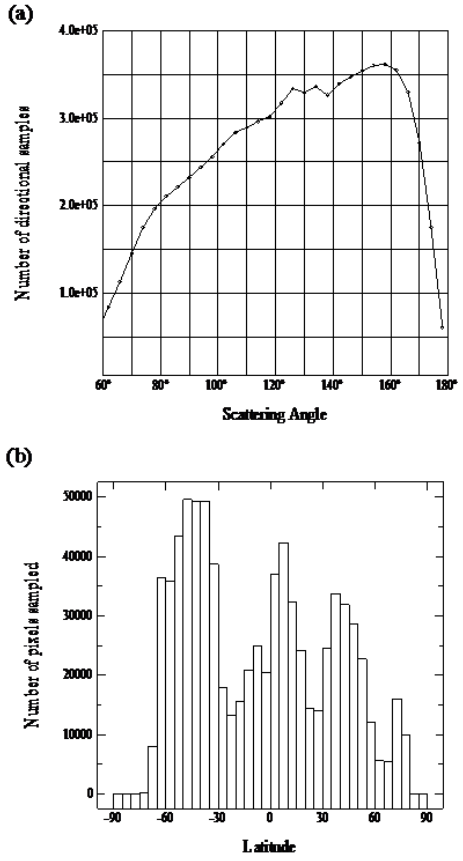

Figure 2. (a) Angular distribution and, **(b)** latitude distribution of the sample pixels.

ACPD
15, 31665–31703, 2015

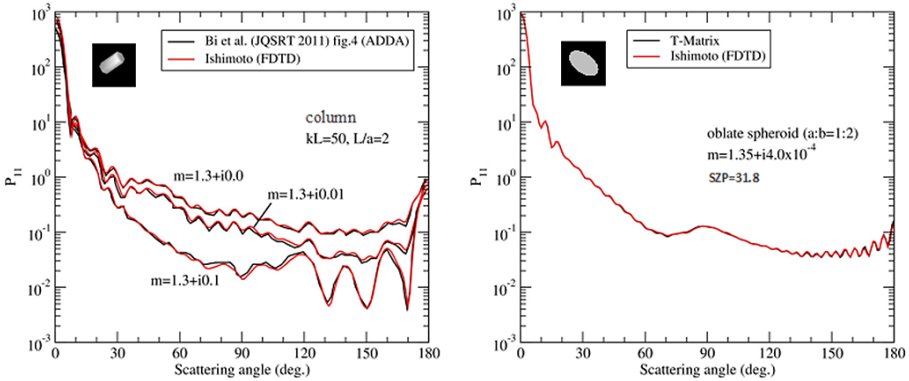

Figure 3. Comparison of the phase functions of randomly oriented column and spheroid particle from FDTD, **T**-matrix and ADDA method.

ACPD
15, 31665–31703, 2015

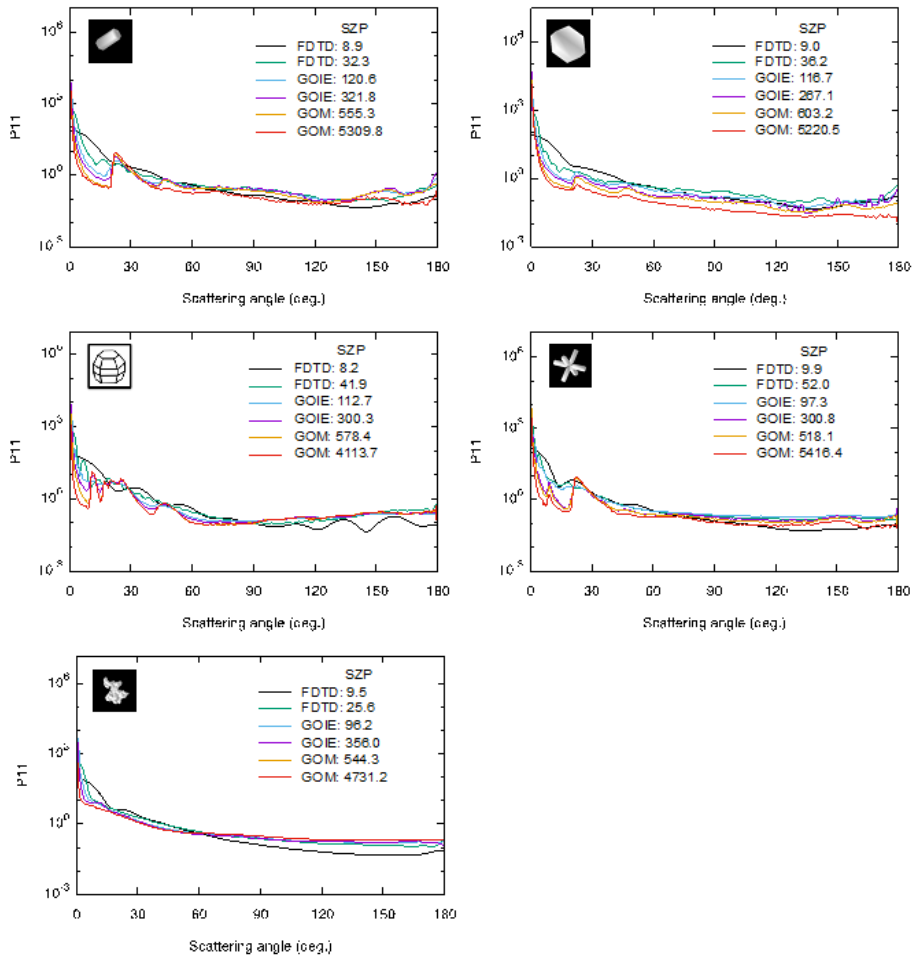

Figure 4. Phase functions of the column, droxtal, plate, bullet rosette and voronoi habit employed in this study with various size parameters at wavelengths of 0.686 µm.

ACPD
15, 31665–31703, 2015

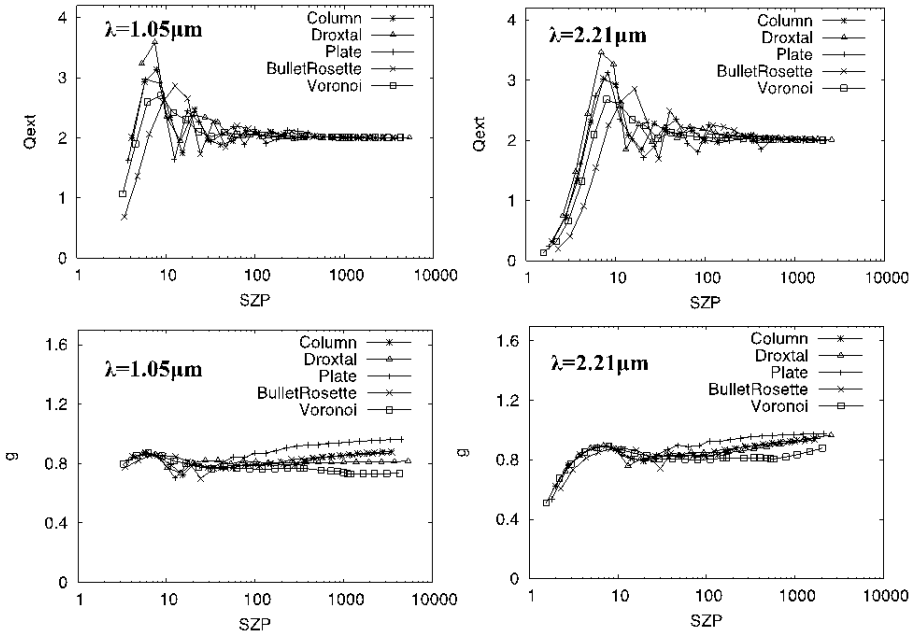

Figure 5. Comparison of the single scattering property of the various ice crystals models computed in this study at wavelength of 1.05 and 2.21 μm.

ACPD
15, 31665–31703, 2015

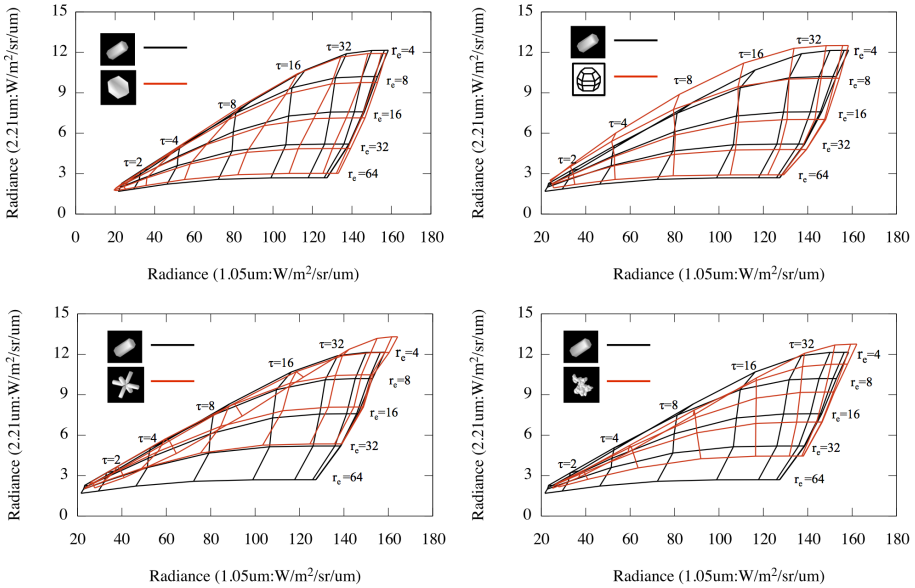

Figure 6. Comparison of the satellite observed radiance with various ice crystal models. (Solar zenith angle: 40°, Satellite zenith angle: 30°, azimuth angle: 90°, Atmospheric model: US-Standard Atmospheric, Surface Albedo: 0.1 (Lambert)).

ACPD
15, 31665–31703, 2015

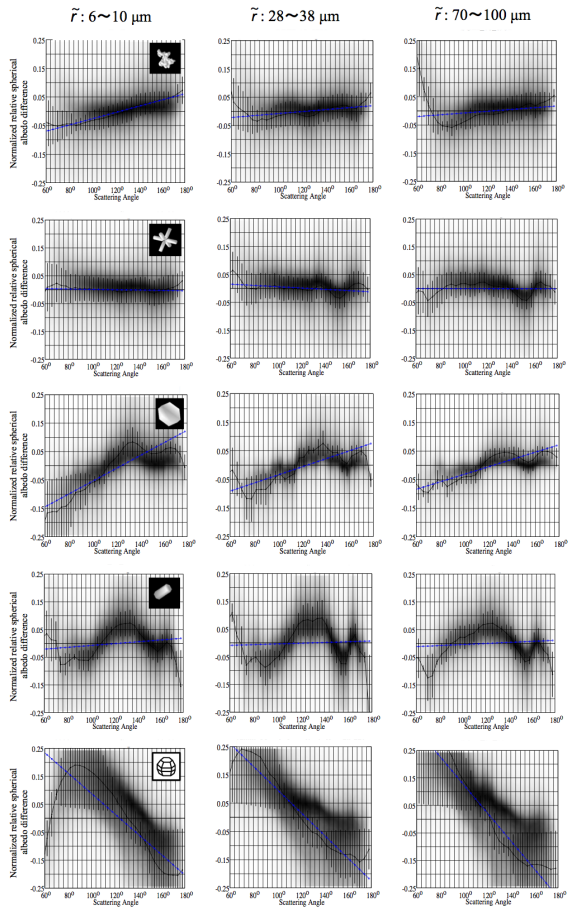

Figure 7. SAD analysis as a function of different particle habits and effective particle radius using POLDER measurement.

ACPD
15, 31665–31703, 2015

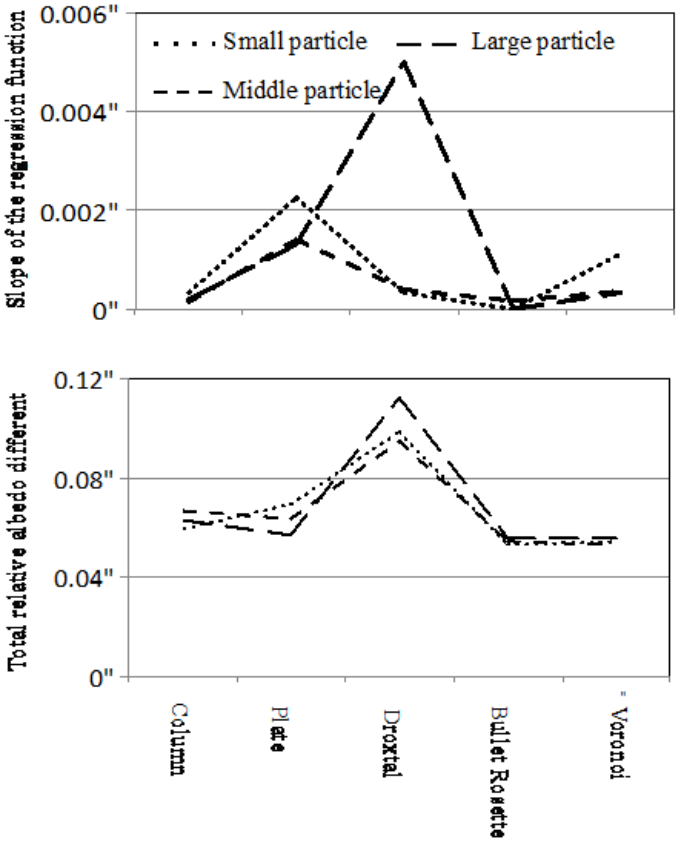

Figure 8. The slope of the regression function and total relative albedo different in Fig. 7.

ACPD
15, 31665–31703, 2015

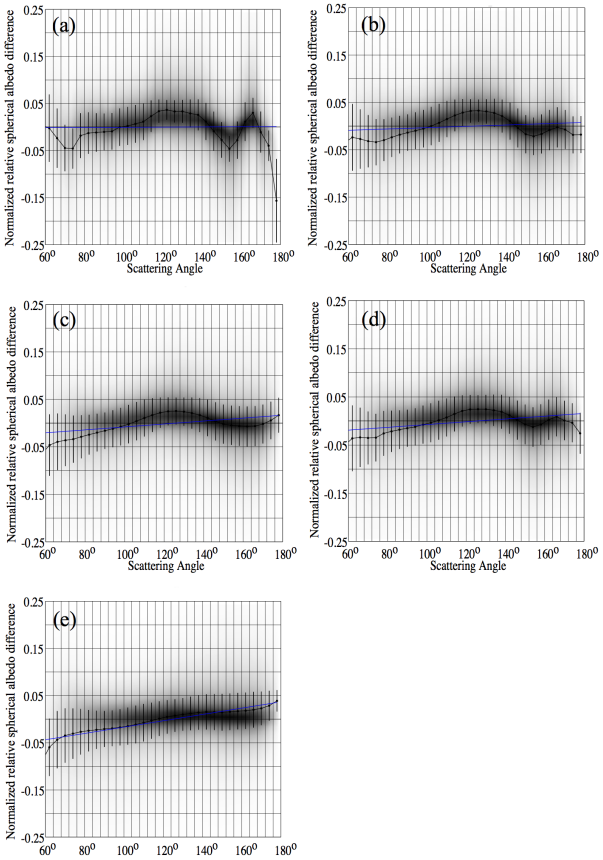

Figure 9. SAD analysis of the Ensemble ice particle model with $\widetilde{r} = 30\,\mu m$ for various distortions: **(a)** no distortion applied; **(b)** with distortion value of 0.15; **(c)** with distortion value of 0.25; **(d)** averaged over all distortion values; **(e)** distortion value of 0.4 is assumed with spherical air inclusions.

ACPD
15, 31665–31703, 2015

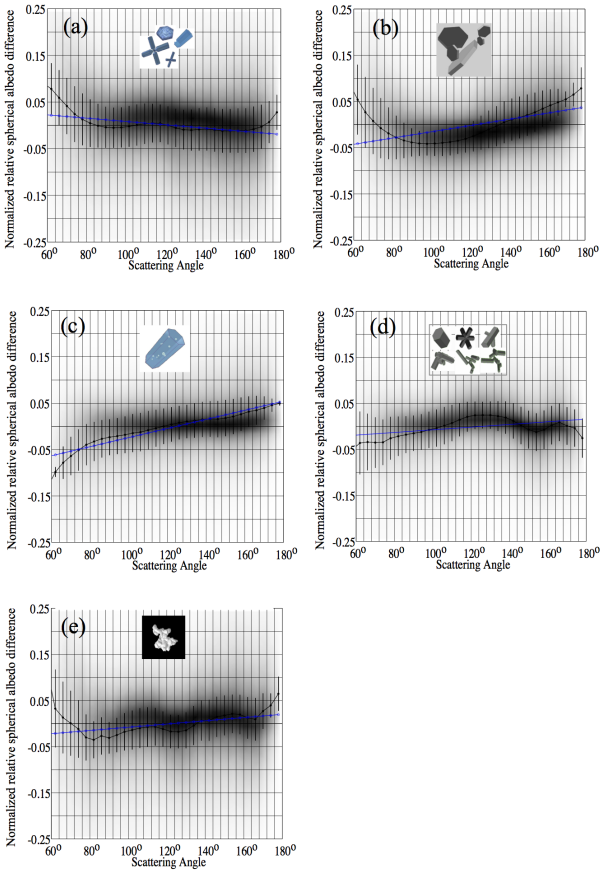

Figure 10. Comparison of the SAD analysis for various ice particle models with $\tilde{r} = 30\,\mu m$: **(a)** GHM with rough surface; **(b)** 5-plate aggregate with rough surface; **(c)** IHM smooth; **(d)** Ensemble ice particle model with averaged over all distortions values; **(e)** Voronoi smooth.

ACPD
15, 31665–31703, 2015

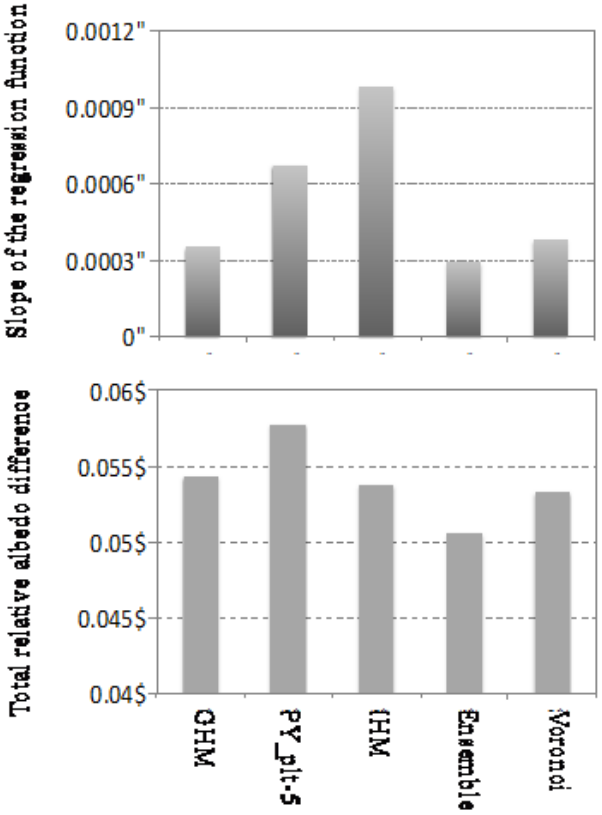

Figure 11. The slope of the regression function and total relative albedo difference for various ice particle models in Fig. 10.

ACPD
15, 31665–31703, 2015